RSC Advances

PAPER

View Article Online
View Journal | View Issue

Cite this: *RSC Adv.*, 2026, **16**, 27756

Enzymatic electrochemiluminescence sensor based on a ternary luminol–H_2O_2-confined nanocatalyst system for sensitive determination of uric acid

Chunchun Wei,[abc] Mixia Chen,[d] Wei Hu,[abc] Fei Yan*[d] and Yu Cui*[abc]

An enzymatic electrochemiluminescence (ECL) sensor based on a ternary luminol system is developed for highly sensitive detection of uric acid (UA). The platform integrates nanochannel-confined platinum nanoparticle (PtNPs) and nitrogen-doped graphene quantum dot (NGQDs) nanocomposites (PtNPs–NGQDs) as coreaction accelerators, with urate oxidase (Uox) covalently immobilized at the nanochannel entrances. In this design, an amino-functionalized vertically ordered mesoporous silica film (NH_2-VMSF) confined the PtNPs–NGQDs within its nanochannels, while Uox is attached to the outer surface. The confined PtNPs–NGQDs exhibit a synergistic catalytic effect, amplifying the ECL signal of the luminol–H_2O_2 system by 16.1-fold. In the presence of UA, immobilized Uox catalyzes its oxidation to generate H_2O_2, which is subsequently decomposed by the PtNPs–NGQDs nanocomposite, leading to enhanced ECL emission. Under optimized conditions, the sensor exhibits two linear response ranges for UA (0.01–1 μM and 1–50 μM) and a low detection limit of 8.1 nM (S/N = 3). The sensor also demonstrates good selectivity and stability, enabling reliable UA quantification in complex urine samples. This work provides a simple and versatile strategy for constructing sensitive ECL enzymatic platforms suitable for the detection of metabolites.

Received 13th March 2026
Accepted 5th May 2026

DOI: 10.1039/d6ra02118b

rsc.li/rsc-advances

1. Introduction

Uric acid (UA), the final metabolic product of purine catabolism in humans, is primarily eliminated through renal excretion.[1] Dysregulation of UA metabolism, resulting from either excessive production or insufficient excretion, leads to elevated serum UA levels and eventually hyperuricemia.[2] Commonly, UA monitoring is closely associated with renal pathophysiology through a bidirectional relationship. On one hand, the kidney serves as the principal organ responsible for UA clearance; impairment of renal function reduces UA excretion and consequently increases serum UA levels, producing secondary hyperuricemia.[3] Under such circumstances, UA measurement provides a sensitive indicator of renal excretory dysfunction. On the other hand, persistent hyperuricemia is recognized as an independent risk factor for kidney injury. Deposition of urate crystals in renal tubules and interstitial tissues can induce inflammatory responses and fibrosis, resulting in urate nephropathy, while crystal aggregation may also lead to urinary tract obstruction and renal damage.[4] Therefore, reliable determination of UA is of great significance for diagnosing hyperuricemia, assisting in the differentiation and monitoring of chronic kidney disease, and evaluating the risk of UA-related renal impairment.

At present, various analytical approaches have been developed for UA determination, including colorimetric assays,[5] chemiluminescence,[6] and electrochemical (EC) analysis.[7] Despite their widespread use, these techniques still suffer from certain limitations in terms of analytical efficiency and operational convenience. For example, colorimetric assays are susceptible to interference from the intrinsic color of biological samples. The sensitivity of chemiluminescence methods should be further improved. EC detection is commonly limited by the interference of redox substances in complex matrix. Development of facile and sensitive method for UA detection is highly desirable.

Electrochemiluminescence (ECL), which integrates electrochemical control with chemiluminescent signal generation, has emerged as a powerful analytical technique.[8–10] As ECL requires no external excitation, it exhibits extremely low background signals and excellent controllability, making it particularly attractive for sensitive detection.[11–13] Luminol is the most widely employed ECL luminophores because of its low cost, excellent aqueous solubility and low ECL potential.[14] However, its

[a]*Kidney Disease Center, The First Affiliated Hospital, Zhejiang University School of Medicine, China. E-mail: cuiyu@zju.edu.cn*

[b]*Institute of Nephrology, Zhejiang University, China*

[c]*Zhejiang Clinical Research Center of Kidney and Urinary System Disease, China*

[d]*School of Chemistry and Chemical Engineering, Zhejiang Sci-Tech University, Hangzhou 310018, P. R. China. E-mail: yanfei@zstu.edu.cn*

intrinsic emission efficiency is relatively limited, and thus binary ECL systems are commonly constructed to improve the ECL intensity. In such systems, luminol is electrochemically oxidized at the electrode surface to form luminol radical anions, which subsequently react with reactive oxygen species (ROS) generated from the decomposition of coreactant (*e.g.* H_2O_2), producing excited-state intermediates that emit light upon returning to the ground state.[15–17] In recent years, the introduction of coreactant promoters to construct ternary ECL systems has been demonstrated as an effective strategy for further enhancing the luminol emission efficiency.[18–21] These coreactant promoters accelerate the generation of ROS from the coreactant, thereby significantly amplifying the ECL response.

To date, various nanocatalysts have been explored as efficient coreactant promoters.[22–24] Noble metal nanomaterials[25] and carbon-based nanostructures such as graphene quantum dots (GQDs)[26] have attracted extensive attention because of their outstanding catalytic properties. For instance, platinum nanoparticles (PtNPs) have large specific surface area as well as abundant active sites, enabling efficient catalytic activity.[27] Meanwhile, GQDs, as zero-dimensional carbon nanomaterials, exhibit unique π–π conjugated structures and edge-active sites, which also contribute to their favorable catalytic activity.[28,29] The integration of these two nanomaterials is expected to generate synergistic effects in electron transfer, active-site enrichment, and structural stability, thereby improving the performance of luminol-based ternary ECL systems. Nevertheless, direct immobilization of nanocatalysts on electrode surfaces often suffers from insufficient exposure of active sites and poor long-term stability. Consequently, the development of strategies to fabricate highly active and stable nanocatalytic systems remains essential for enhancing luminol ECL efficiency.

Confining nanocatalysts within porous materials is effective to enhance both catalytic activity and stability.[30–32] Porous matrices provide a large surface area that facilitates the formation of highly dispersed nanomaterials, thereby exposing more catalytic active sites.[33–35] Meanwhile, the confined microenvironment can effectively prevent nanoparticle aggregation or detachment, preserving catalytic activity and structural stability.[36,37] Vertically ordered mesoporous silica film (VMSF) offers a promising platform for nanocatalyst confinement owing to their well-defined nanochannel architecture.[38–40] This film possesses highly uniform nanochannel diameters (approximately 2–3 nm) with ultrahigh density.[41,42] In addition, the abundant silanol groups on the outer surface enable convenient functionalization, allowing biomolecules such as enzymes to be immobilized and facilitating the construction of highly sensitive biosensing interfaces.[43–45] VMSF film can be readily fabricated over large areas *via* the Stöber solution-growth method[46,47] or rapidly deposited using the electrochemically assisted self-assembly (EASA) technique.[48–50] Thus, VMSF-modified electrodes exhibit considerable promise for constructing biosensing platforms in which catalysts are spatially confined, thereby enabling highly efficient and sensitive detection of UA.

In this work, an amino-functionalized VMSF (NH_2-VMSF) was rapidly prepared on ITO electrode *via* the EASA method. Nitrogen-doped graphene quantum dots (NGQDs) were subsequently confined inside the nanochannels through electrophoretic deposition, followed by *in situ* electrochemical deposition of PtNPs to form PtNPs–NGQDs composite nanocatalysts within the nanochannels. Urate oxidase (Uox) was further covalently immobilized on the outer surface of NH_2-VMSF to construct an enzyme-based sensing interface. In the presence of UA, Uox catalyzed the oxidation of UA to produce H_2O_2 at the electrode surface. The generated H_2O_2 was then efficiently converted into abundant ROS through the synergistic catalytic action of nanochannel-confined PtNPs and NGQDs, which remarkedly enhanced the luminol ECL emission. Based on this mechanism, a highly sensitive ECL sensing strategy for UA determination was achieved. In traditional sensor design, co-immobilizing enzymes and inorganic nanozymes often leads to blocked active sites, severe diffusion barriers, and incompatible microenvironments. This work realized "outer-recognition and inner-amplification" architecture with high performance through nanoconfinement. On the one hand, Uox is immobilized on the outer surface, overcoming the steric hindrance of nanochannels and ensuring rapid, unhindered recognition of UA. On the other hand, the PtNP–NGQD nanocatalyst is confined within the nanochannels, serving as an isolated, highly active and stable ECL amplification zone. The proposed platform offers facile fabrication procedure and significantly amplified ECL signals, thereby providing potential for UA detection.

2. Materials and methods

2.1 Chemical and materials

Urate oxidase (Uox), uric acid (UA), ascorbic acid (AA), tetraethoxysilane (TEOS), cetyltrimethylammonium bromide (CTAB), $Na_2HPO_4 \cdot 12H_2O$, hexaammineruthenium(III) chloride ($Ru(NH_3)_6Cl_3$), bovine serum albumin (BSA), $K_4Fe(CN)_6$, $NaH_2PO_4 \cdot 2H_2O$, $K_3Fe(CN)_6$, ferrocene methanol (FcMeOH), $H_2PtCl_6 \cdot 6H_2O$, luminol, *p*-benzoquinone (BQ), *tert*-butanol (TBA), potassium hydrogen phthalate (KHP), NaOH, KNO_3, KCl, H_2O_2, and glucose (Glu) were purchased from Aladdin Biochemical Technology Co., Ltd (Shanghai, China). Indium tin oxide (ITO, 0.5 cm × 1 cm) was used as conductive electrode. All reagents were of analytical grade and ultrapure water was employed.

2.2 Measurements and instrumentations

TEM (HT7700, Hitachi) operated at 100 kV was used to characterize NH_2-VMSF morphology. For TEM analysis, the film was mechanically detached from ITO, dispersed in ethanol by ultrasonication, and drop-cast onto copper grid. Surface and cross-sectional structures of modified electrodes were examined using SEM (SU8010, Hitachi) at 5 kV. Fluorescence images were obtained with a confocal laser scanning microscope (CLSM, FV1000, Olympus Corporation) using 488 nm excitation. Electrochemical experiments were performed on an Autolab PGSTAT302N workstation (Metrohm, Switzerland), including cyclic voltammetry (CV) and electrochemical impedance spectroscopy (EIS). ECL signals were recorded using an MPI-E II ECL

system. Conventional three-electrode configuration with ITO (bare or modified) as the working electrode, Pt as the counter electrode, and Ag/AgCl (saturated KCl) as the reference electrode were used for electrochemical and ECL measurements. X-ray photoelectron spectroscopy (XPS, PHI5300, Physical Electronics) was used to determine elemental composition (250 W, 14 kV, Mg Kα radiation). UV-vis spectra were obtained on UV-2450 spectrophotometer (Shimadzu Corporation, Japan).

2.3 Fabrication of the enzyme electrode

Grown of NH_2-VMSF on ITO was performed using electrochemically assisted self-assembly (EASA) method according to previously reported procedures.[51] CTAB, TEOS, and APTES were dissolved in an ethanol–$NaNO_3$ solution to form the precursor solution (pH 2.97) and the solution was stirred for 2.5 h to promote siloxane hydrolysis. Then, ITO electrode was immersed and electrolysis at −350 μA was performed for 10 s. The rinsed electrode was aged at 120 °C for 12 h to obtain SM@NH_2-VMSF/ITO. After incubating in 5% glutaraldehyde (GA, 0.01 M PBS) at 37 °C for 20 min, the aldehyde-modified electrode was obtained. The surfactant template was removed by stirring in HCl/ethanol solution for 5 min, yielding open nanochannel modified electrode (GA/NH_2-VMSF/ITO). NGQDs were confined within the nanochannels by electrophoretic deposition at +0.8 V in NGQDs dispersion (10 mg mL^{-1}). Subsequently, Pt nanoparticles were generated *in situ* by electrochemical deposition in H_2PtCl_6 solution (3.86 mM) at −0.2 V, producing PtNPs–NGQDs@NH_2-VMSF/ITO. Finally, the electrode was incubated in Uox solution (2 mg mL^{-1}) at 4 °C for 1 h to immobilize the enzyme followed with incubation in a 1 mg per mL BSA solution to block nonspecific sites, yielding Uox/PtNPs–NGQDs@GA/NH_2-VMSF/ITO. The electrode was stored at 4 °C prior to use.

2.4 ECL detection of UA and analysis of real samples

ECL measurements were performed by CV over a potential range of 0–0.8 V. The scan rate was 100 mV s^{-1}. Before detection, the enzyme electrode was incubated in UA solutions at 37 °C for 60 min to allow enzymatic reaction. Unless otherwise stated, measurements were conducted luminol solution (100 μM in 0.01 M PBS, pH 8). ECL signals and CV curves were simultaneously recorded at room temperature with a PMT voltage of 750 V. The analytical applicability of the sensor was evaluated when UA was detected in human urine (the samples came from volunteers, and informed consent was obtained for the sample testing experiments.) with standard addition method. Urine samples or spiked samples were diluted with PBS (0.01 M, pH 8.0) prior to measurement.

3. Results and discussion

3.1 Construction strategy of enzyme sensor and mechanism for UA detection

The fabrication procedure of the Uox-based ECL sensor and the corresponding UA sensing principle are illustrated in Fig. 1. VMSF functionalized with amino groups (NH_2-VMSF) were grown on ITO electrodes *via* EASA method. During the cathodic

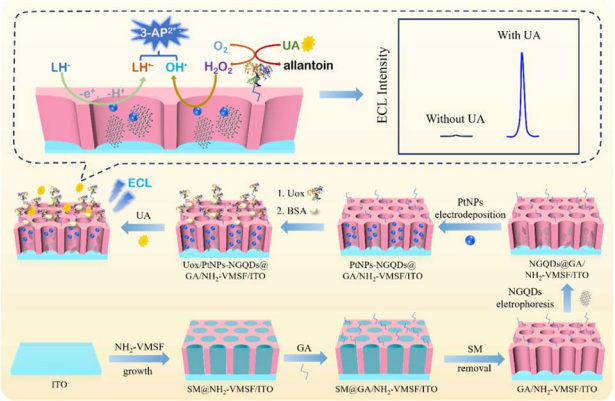

Fig. 1 Schematic illustration of the preparation of the enzyme-based sensor for UA detection.

polarization process in EASA method, reduction of protons or water occurred at the electrode surface, generating a localized increase in pH. This interfacial pH gradient triggered the cooperative self-assembly of surfactant micelles (SM) together with hydrolysis and condensation of siloxane precursors, resulting in the formation of silica nanochannels containing SM templates (SM@NH_2-VMSF/ITO). To enable covalent fixation of Uox on the outer surface (entrance of nanochannels), aldehyde groups were introduced through glutaraldehyde (GA) modification. This step was performed prior to surfactant removal in order to avoid crosslinking reactions within the nanochannels. Negatively charged NGQDs were then electrophoretically introduced into the nanochannels. Afterwards, PtNPs were *in situ* electrochemically deposited in nanochannels to yield confined PtNPs–NGQDs nanocomposites. Subsequent extraction of the surfactant template in an ethanol/HCl solution easily generated open nanochannels. Finally, Uox was covalently anchored onto the outer surface through Schiff-base coupling between enzyme amino groups and aldehyde functionalities, resulting in the Uox/PtNPs–NGQDs@GA/NH_2-VMSF/ITO enzyme electrode.

For UA detection, luminol served as the ECL luminophore, while H_2O_2 produced by the Uox-catalyzed oxidation of UA acted as the coreactant. The PtNPs–NGQDs nanocomposite confined inside the nanochannels efficiently catalyzed H_2O_2 decomposition to generate reactive oxygen species (ROS), which markedly amplified the luminol ECL emission. In this architecture, the enzyme recognition interface was spatially located on the outer surface of the silica film, whereas catalytic amplification occurred inside the nanochannels. Such spatial separation ensured efficient enzymatic recognition while maintaining high catalytic activity and stability of the nanocatalysts, thereby enabling sensitive UA detection.

3.2 Characterization of NH_2-VMSF and PtNPs–NGQDs@NH_2-VMSF electrodes

The morphology of NH_2-VMSF were characterized by TEM and SEM. The top-view TEM image (Fig. 2A) revealed highly ordered hexagonal arrangement of nanochannels with a pore density of

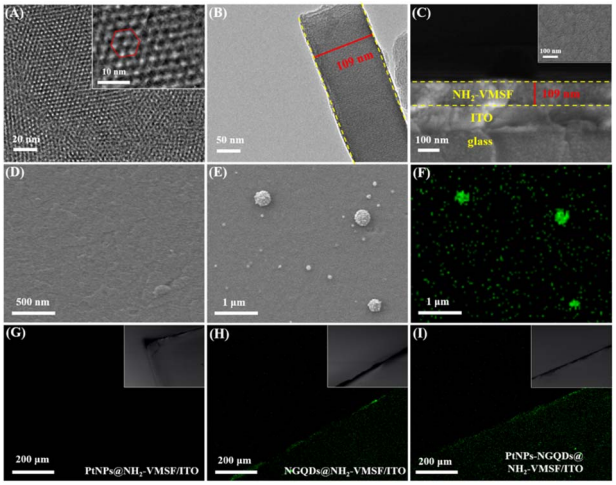

Fig. 2 (A) TEM surface image of NH_2-VMSF/ITO. (B) TEM cross-sectional image of NH_2-VMSF/ITO. (C) SEM cross-sectional image of NH_2-VMSF/ITO, with the inset showing the SEM surface image. (D) SEM surface image of PtNPs–NGQDs@NH_2-VMSF/ITO. (E) SEM surface image of PtNPs–NGQDs@NH_2-VMSF/ITO after removal of NH_2-VMSF. (F) Elemental mapping of Pt corresponding to (E). (G–I) CLSM images of different electrodes under bright-field and dark-field conditions (insets), with an excitation wavelength of 488 nm.

approximately 75 000 pores μm^{-2} and a uniform pore (nanochannel) diameter of 2–3 nm. TEM image of the cross-sectional (Fig. 2B) further confirmed the long-range ordered channel structure, with a measured film thickness of approximately 109 nm. SEM analysis (Fig. 2C) showed a well-defined multilayer structure consisting of the NH_2-VMSF layer, conductive ITO layer, and glass substrate. Silica-based NH_2-VMSF had uniform thickness and smooth morphology without detectable silica aggregates. The SEM surface image (inset in Fig. 2C) indicated that the film remained intact.

To verify the successful confinement of PtNPs–NGQDs inside the nanochannels, additional SEM characterization was performed. As shown in Fig. 2D, the surface morphology of PtNPs–NGQDs@NH_2-VMSF/ITO remained nearly identical to that of NH_2-VMSF/ITO, suggesting that the nanomaterials were not deposited on the outer surface. After etching the NH_2-VMSF framework with NaOH solution, however, numerous aggregated nanoparticles appeared on the electrode surface (Fig. 2E). Elemental mapping analysis (Fig. 2F) confirmed the presence of Pt within these particles. This indicated that PtNPs were originally confined within the nanochannels. Once the NH_2-VMSF framework was removed, the spatial confinement was lost, leading to catalyst aggregation.

The cyclic voltammogram of PtNPs–NGQDs@NH_2-VMSF/ITO electrode in 0.5 M H_2SO_4 was shown in Fig. S1 (SI). The typical characteristics of Pt-related electrode in acidic media were observed including peaks in low-potential region (deposition/desorption of H_2 on Pt surface), high-potential region (the formation of hydroxyl/oxide species), and the reduction peak observed during the reverse scan (reduction of surface platinum oxides). These results indicated the success confinement of PtNPs in nanochannels. The intrinsic fluorescence of NGQDs was exploited to evaluate their effective confinement within the nanoporous framework. Confocal laser scanning microscopy (CLSM) was performed on the various modified electrodes using an excitation wavelength of 488 nm (Fig. 2G–I). Bright-field images and the corresponding bright-field images (Insets) are presented. The PtNPs@NH_2-VMSF/ITO electrodes, which lacked confined NGQDs, exhibited no detectable fluorescence, confirming that neither the NH_2-VMSF nor the deposited Pt nanoparticles possess intrinsic emissive properties. By contrast, the NGQDs@NH_2-VMSF/ITO and PtNPs–NGQDs@NH_2-VMSF/ITO electrodes, incorporating spatially restricted NGQDs, demonstrated pronounced green fluorescence localized on the electrode surface. For comparison, NH_2-VMSF/ITO electrode was immersed in NGQDs solution without electrophoretic deposition. The electrode was then washed and observed, showing no fluorescence signal from NGQDs (Fig. S2 in SI). This confirms that NGQDs cannot adsorb onto the outer surface or passively diffuse into the channels. These results proved that the NGQDs were successfully immobilized within the nanochannels through electrophoretic deposition.

XPS was employed to analyze the elemental composition of the electrode surface. Fig. S3A (SI) showed the XPS survey spectra of NH_2-VMSF/ITO and PtNPs–NGQDs@NH_2-VMSF/ITO. In the survey spectrum of NH_2-VMSF/ITO, characteristic peaks of Si 2p, Si 2s, C 1s, N 1s, and O 1s can be observed. The Si and O characteristic peaks originate from the SiO_2 framework, while the N 1s peak arises from the amino groups in NH_2-VMSF. After PtNPs–NGQDs confinement within the nanochannels, Pt 4f peak appeared. The high-resolution Pt 4f spectrum (Fig. S3B, SI) shows a doublet that is in good agreement with the standard data for metallic Pt^0, confirming the successful deposition of PtNPs. In the high-resolution N 1s spectrum (Fig. S3C, SI), the N content of the electrode after confined modification increased compared to that of the NH_2-VMSF/ITO electrode. This increase originated from the NGQDs deposited within the nanochannels, demonstrating successful confinement of NGQDs. These results further prove the successful confinement of PtNPs–NGQDs in nanochannels.

3.3 Synergistic enhancement of ECL by confined PtNPs–NGQDs

The ECL responses of different modified electrodes were examined to evaluate the catalytic performance of the confined nanomaterials. As shown in Fig. 3A and B, the NH_2-VMSF/ITO electrode generated only a weak ECL signal, indicating that the silica nanochannel film itself did not significantly promote luminol emission. When PtNPs were confined inside the nanochannels, the ECL intensity increased remarkedly due to their excellent catalytic activity toward H_2O_2 decomposition. Similarly, NGQDs-modified electrodes also exhibited enhanced ECL emission, which could be attributed to their favorable catalytic activity. Confined PtNPs–NGQDs exhibited an amplified ECL signal of the luminol–H_2O_2 system by 16.1-fold. More importantly, the electrode containing both PtNPs and NGQDs displayed a significantly stronger ECL signal than electrodes

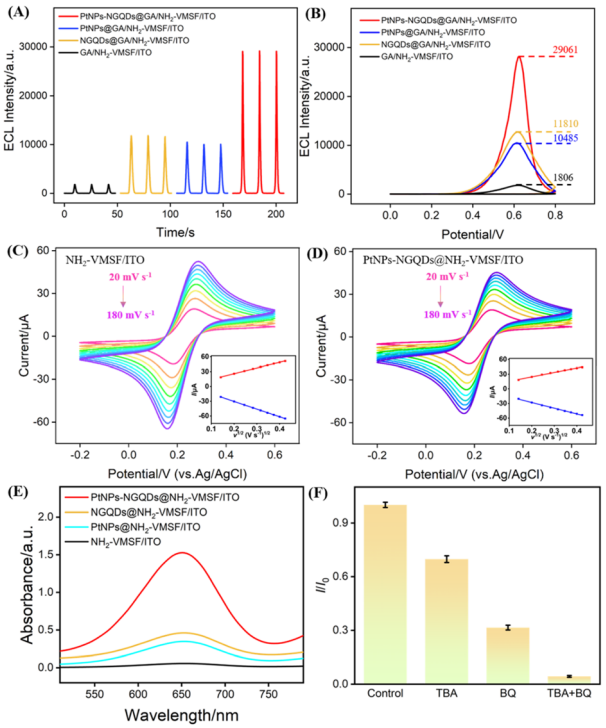

Fig. 3 (A) ECL-time curves of different electrodes. (B) ECL-potential curves of various electrodes. (C and D) CV curves of NH_2-VMSF/ITO (C) and PtNPs–NGQDs@NH_2-VMSF/ITO (D) in 0.5 mM FcMeOH solution. Insets show the corresponding linear fits of the peak current (I) *vs.* the square root of the scan rate ($v^{1/2}$). (E) UV-vis absorption spectra obtained using different electrode. Test conditions: 0.1 M NaAc/HAc buffer containing 1 mM H_2O_2 and 0.5 mM TMB, pH = 4. (F) ECL signal obtained on PtNPs–NGQDs@NH_2-VMSF/ITO electrode in presence or absence of different radical scavengers. I and I_0 represent the ECL signals in the presence and absence of radical scavenger, respectively.

modified with either component alone, suggesting a synergistic catalytic interaction between PtNPs and NGQDs.[52,53]

The observed enhancement in ECL signals could originate either from an increase in electroactive surface area or from improved catalytic activity. To investigate the mechanism, the influence of the electroactive area on signal variation was first investigated. Neutral ferrocene methanol (FcMeOH) was selected as the electrochemical probe, and CV measurements were performed at varying scan rates on NH_2-VMSF/ITO and PtNPs–NGQDs@NH_2-VMSF/ITO electrodes. The CV curves (I) and the corresponding linear plots of peak current *versus* the square root of the scan rate ($v^{1/2}$) are shown in Fig. 3C and D. As the scan rate increased, the peak currents also increased, and the linear fits demonstrated a good linear relationship between the peak current and the square root of the scan rate, indicating that the diffusion process governs the electron transfer in both electrode systems. The electroactive surface area of each electrode was calculated using the Randles–Sevcik equation.[54] Compared with the electrode prior to confinement, the PtNPs–NGQDs confined within the nanochannels exhibited a 21.6% decrease in electroactive area. This reduction is attributed to hindered diffusion of the probe molecules and increased interfacial resistance caused by the immobilized nanocomposites within the nanochannels. These results confirm that the enhancement of the ECL signal is not due to an increase in electroactive surface area.

To investigate the signal-enhancing mechanism of the PtNPs–NGQDs nanocatalyst on the luminol-based ternary ECL system, the nanozyme activity of PtNPs–NGQDs was evaluated. Using 3,3′,5,5′-tetramethylbenzidine (TMB) as the chromogenic substrate, the four types of electrodes were incubated in an acetate buffer containing H_2O_2, and the absorbance of the oxidation product, oxidized TMB (oxTMB), was measured at 652 nm. The corresponding UV-visible spectra are presented in Fig. 3E. The NH_2-VMSF/ITO electrode exhibited a low absorbance at 652 nm, indicating negligible catalytic activity. Electrodes with a single nanozyme confined within the nanochannels showed significantly enhanced absorbance, demonstrating that both PtNPs and NGQDs possess inherent catalytic activity. Notably, the electrode incorporating the PtNPs–NGQDs nanocomposite within the nanochannels displayed the highest absorbance, confirming a synergistic catalytic effect that efficiently promotes H_2O_2 decomposition to generate reactive oxygen species (ROS) and subsequently accelerate oxTMB formation.

To identify the active ROS involved in the ECL process, different radical scavengers were employed. Fig. 3F compare the ECL responses of NH_2-VMSF/ITO and PtNPs–NGQDs@NH_2-VMSF/ITO electrodes in luminol solutions containing various scavengers. The PtNPs–NGQDs@NH_2-VMSF/ITO electrode exhibited partial quenching of the ECL signal upon addition of either *tert*-butanol (TBA, an $^{\bullet}OH$ scavenger)[55,56] or *p*-benzoquinone (BQ, an $O_2^{\bullet-}$ scavenger)[57] individually, and nearly complete quenching when both scavengers were present simultaneously, revealing the coexistence of both hydroxyl radicals ($^{\bullet}OH$) and superoxide radicals ($O_2^{\bullet-}$).

Thus, the confinement of PtNPs–NGQDs hinders probe diffusion and increases the interfacial resistance, rather than facilitating electron-transfer kinetics. The ECL increase is mainly attributed to the nanozyme-like catalytic decomposition of H_2O_2 by PtNPs–NGQDs, which generates abundant ROS to promote the luminol ECL process. The proposed ECL mechanism of this system is as follows: luminol undergoes deprotonation to form the electroactive luminol anion (LH^-), which is subsequently oxidized at the electrode surface to generate the luminol radical anion ($L^{\bullet-}$). The PtNPs–NGQDs nanocomposite catalyzes H_2O_2 decomposition, producing abundant $^{\bullet}OH$ radicals. The reaction between $L^{\bullet-}$ and $^{\bullet}OH$ generates the excited-state 3-aminophthalate (AP^{2-}*), which relaxes to the ground state with emission.

3.4 Verification of enzyme sensor fabrication

The interfacial properties of electrodes at different stages of enzyme sensor fabrication were examined using CV and EIS. Fig. 4A and B presents CV curves and EIS plots of various modified electrodes using $Fe(CN)_6^{3-/4-}$ redox probe. In comparison with NH_2-VMSF/ITO electrode (oxidation peak: 120.5 μA, reduction peak: 129.3 μA, charge transfer resistance-

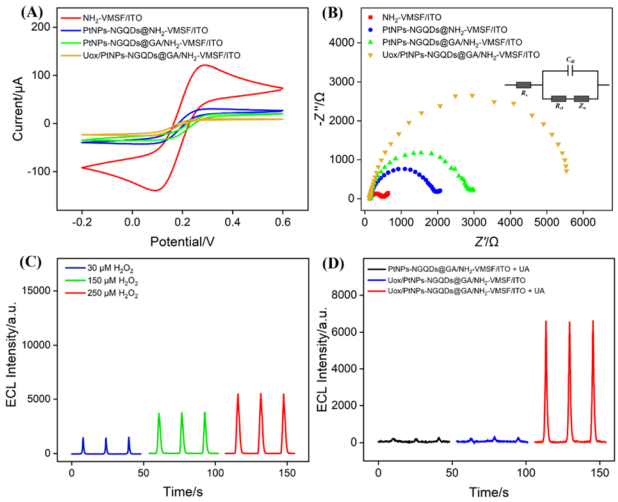

Fig. 4 (A) CV curves and (B) EIS plots of different electrodes. The solution was 0.1 M KCl solution containing 2.5 mM $Fe(CN)_6^{3-/4-}$. The inset in (B) shows the schematic diagram of the equivalent circuit. (C) ECL signal response of the enzyme electrode in a luminol detection solution with different H_2O_2 concentrations. (D) ECL signals of different electrodes in luminol (100 μM) without or with 10 μM UA.

R_{ct}: 496 Ω), a remarked decrease in peak current (oxidation peak: 29.5 μA, reduction peak: 34.7 μA) and a significant increase in R_{ct} (1948 Ω) were observed upon confinement of PtNPs–NGQDs within the nanochannels, attributable to the decreased electron-transfer kinetics resulting from the restricted diffusion of the electroactive probe toward the electrode surface and the elevated interfacial resistance induced by the confined nanocatalysts. Following glutaraldehyde (GA) crosslinking, the peak current decreased slightly (oxidation peak: 18.8 μA, reduction peak: 29.9 μA) while R_{ct} increased (2849 Ω), reflecting the formation of a partially insulating layer on the electrode surface by GA, which hindered electron transfer. Subsequent immobilization of Uox further reduced the peak current (oxidation peak: 9.6 μA, reduction peak: 21.6 μA) and markedly increased R_{ct} (5538 Ω), resulting from the steric hindrance imposed by the enzyme macromolecules and the nonconductive nature of the protein, which amplified the diffusion limitations of the probe molecules. These observations confirmed the successful confinement of nanocatalysts and the effective immobilization of Uox.

3.5 Feasibility verification of UA detection *via* enzymatically generated H_2O_2

For quantitative analysis of UA, Uox catalyzed UA to generate H_2O_2, enabling indirect detection of UA. As shown in Fig. 4C, the Uox/PtNPs–NGQDs@NH_2-VMSF/ITO electrode exhibited a gradual increase in ECL intensity with rising H_2O_2 concentration. Then, feasibility of UA detection *via* enzymatically generated H_2O_2 was vitrificated. Fig. 4D compares the ECL responses of electrodes with different modifications in the presence or absence of UA. Electrodes without Uox modification generated only negligible ECL signals in UA-containing systems. Electrodes modified with Uox produced no detectable signal in UA-free systems, excluding interference from non-specific reactions. Only the Uox-modified electrode in UA-containing systems generated a significant ECL response, demonstrating that the enzyme–substrate specific recognition was essential for producing H_2O_2 from UA. The H_2O_2 was subsequently catalyzed by PtNPs–NGQDs to generate ROS, which promoted luminol ECL and shows potential for UA detection.

3.6 Optimization of fabrication conditions for the enzyme sensor

To enhance the signal intensity of the electrode and improve the sensitivity of the sensor, the fabrication conditions for the enzyme electrode including the electrophoretic deposition time of NGQDs or PtNPs were optimized. Fig. 5 illustrates the optimization process for constructing the PtNPs–NGQDs composite interface. As shown in Fig. 5A, with a fixed PtNPs electrodeposition time of 2 s, the ECL signal progressively increased with the extension of NGQDs electrophoretic time. The ECL intensity reached its peak when the electrophoretic time was 90 s, beyond which further extension led to a decrease in the ECL signal. This may be attributed to the fact that while an increased amount of deposited NGQDs enhances catalytic activity, an excessive amount may decrease the diffusion of the luminophore.

Fig. 5B demonstrates that under the optimal NGQDs electrophoretic time of 90 s, the ECL signal continuously increased with increasing PtNPs electrodeposition time. The maximum ECL intensity was achieved at an electrodeposition time of 2 s, after which the signal began to decrease. Excessive deposition time might cause large PtNPs to readily obstruct the nanochannels, thereby hindering luminol diffusion and ultimately leading to a decrease in the ECL signal. Consequently, 2 s for PtNPs electrodeposition were chosen.

3.7 Performance for ECL detection of UA using the fabricated enzyme electrode

Fig. 6 presents the ECL signals of the Uox/PtNPs–NGQDs@GA/NH_2-VMSF/ITO sensor measured in luminol detection solutions containing various concentrations of UA under optimal experimental conditions. As shown in Fig. 6A, the ECL intensity of the

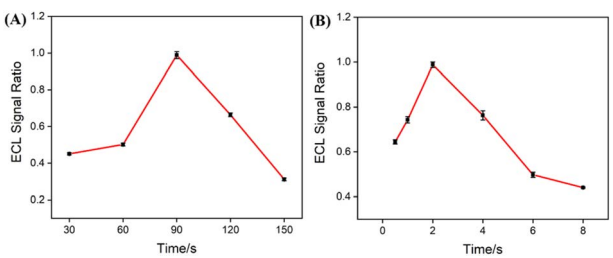

Fig. 5 (A) ECL signals of electrodes obtained with varying NGQDs electrophoretic time, while fixing the PtNPs deposition time at 2 s. (B) ECL signals of electrodes obtained with varying PtNPs electrodeposition time, while fixing the NGQDs electrophoretic time at 90 s. The ECL signal ratio is defined as the ratio of the ECL signal obtained under each condition to the maximum ECL signal achieved.

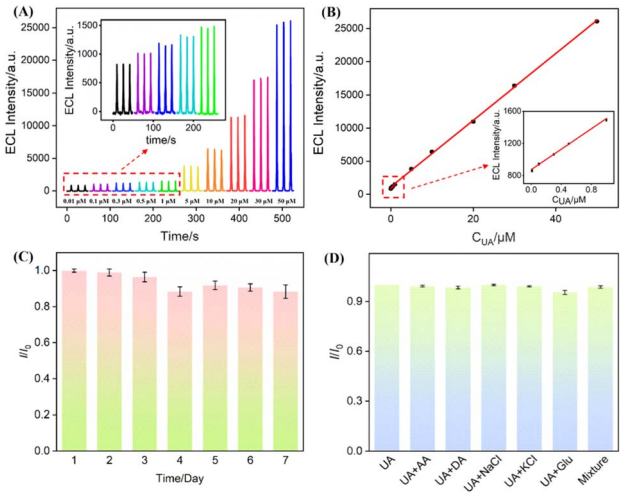

Fig. 6 (A) ECL signal responses of the enzyme electrode for detecting various concentrations of UA. The inset shows the ECL signal responses in low concentrations. (B) Corresponding linear calibration curves. The inset displays an enlarged view of the linear calibration curve in low concentrations. (C) Storage stability of the enzyme electrode. (D) Selectivity and anti-interference performance of the enzyme electrode. The concentrations of interferents were 0.5 μM for AA, 0.01 μM for DA, 1 mM for NaCl, 1 mM for KCl, and 10 μM for Glu.

sensor gradually increased with increased UA concentration. Fig. 6B displays the corresponding linear calibration curves. The ECL signal (I_{ECL}) exhibited a linear relationship with UA concentration (C_{UA}) within the ranges of 0.01–1 μM and 1–50 μM. The linear regression equations were $I_{ECL} = 635.7\ C_{UA} + 872.5$ ($R^2 = 0.997$) and $I_{ECL} = 502.2\ C_{UA} + 1134$ ($R^2 = 0.999$) respectively. The presence of two linear ranges is likely related to a change in the dominant response. At low concentration, the signal is mainly governed by interfacial reaction kinetics with sufficient available active sites, whereas at higher concentration, partial site occupation and increasing mass-transport limitation within the nanochannels lead to a different linear response slope. The detection limit was calculated to be 8.1 nM based on a signal-to-noise ratio of 3 (S/N = 3.3). Compared with other previously reported electrochemical (EC) or ECL sensors, the proposed UA sensor exhibited a lower LOD (Table S1 in SI). The high sensitivity might be ascribed to the confinement of PtNPs–NGQDs that act as highly efficient nanozyme-like coreactant accelerators, promoting the decomposition of H_2O_2 to generate abundant ROS and amplifying the luminol ECL emission. In other words, although the accessible electrochemical area and electron-transfer kinetics were somewhat reduced, the local catalytic efficiency per interfacial site was greatly enhanced, and this positive catalytic effect outweighs the negative impacts.

The fabrication repeatability, storage stability, selectivity, and anti-interference capability of the enzyme sensor were evaluated. Five independently fabricated sensors were employed to detect UA (1 μM), yielding a relative standard deviation (RSD) of 3.7% in the signals, which indicates high fabrication repeatability. Furthermore, a single sensor was used to five consecutive measurements of UA (1 μM) under identical conditions, and the resulting RSD of 2.7% of ECL signals confirms good detection repeatability. Seven sensor electrodes prepared under the same conditions were stored at 4 °C, with one electrode taken daily for UA (1 μM) detection. On the seventh day, the measured ECL signal retained 88% of its initial value (Fig. 6C), demonstrating good storage stability. CV curve of the PtNPs–NGQDs@NH_2-VMSF/ITO electrode was recorded in sulfuric acid after 7 days of storage (Fig. S4, SI). The CV profile was nearly unchanged compared with that of the freshly prepared electrode, indicating that the confined nanocatalysts remained stable. The high stability of the confined nanocatalyst might result from two aspects. (1) Physical barrier: the rigid silica walls physically restrict the migration and aggregation of the confined nanocatalyst, thereby preserving their high specific surface area and active sites over long periods. (2) Anti-fouling based on size-exclusion: The ultra-small nanochannels (2–3 nm) act as an inherent molecular sieve. They effectively block large macromolecules (*e.g.*, proteins) from reaching and fouling the catalyst surface. This ensures the long-term activity. Thus, the signal loss might be ascribed to the enzyme denaturation.

To assess the selectivity and anti-interference performance of the enzymatic sensor for UA detection, common interferents present in biological fluids, including ascorbic acid (AA), dopamine (DA), sodium chloride (NaCl), potassium chloride (KCl), and glucose (Glu), were selected. As shown in Fig. 6D, the detection signal for UA remained largely unaffected even in the presence of the mixture of multiple potential interferents, confirming good selectivity and anti-interference capability of the fabricated enzyme sensor. This performance is primarily attributed to the specific catalytic reaction of Uox towards UA and the inherent antifouling properties of VMSF. While electroactive interferents like DA and AA can easily interfere with conventional electrochemical sensors, our detection mechanism relies on ECL emission of the luminol system triggered by H_2O_2. DA and AA, although electroactive, cannot generate ECL signals under our experimental conditions. Commonly salts including NaCl and KCl also cannot generate ECL signals under the experimental conditions.

3.8 Real sample analysis

The applicability of the fabricated enzymatic sensor for UA detection in real samples was investigated. Urine was selected as the real sample matrix, and UA detection was performed

Table 1 Detection of UA in urine

Sample	Added[a] (μM)	Found[a] (μM)	RSD (%, $n = 3$)	Recovery (%)
Urine	—	1.58	1.1	—
	1.00	2.57	0.9	99.0
	5.00	6.68	1.7	102
	10.0	11.5	1.3	99.2

[a] The concentration was obtained after being diluted.

using the standard addition method (Table 1). The recovery rates ranged from 99.2% to 102%, with RSD no more than 1.7%, demonstrating the high accuracy and reliability of the sensor for UA quantification in complex real sample matrices. The high recovery and low matrix effects are guaranteed by two aspects. On the one hand, the intact NH_2-VMSF layer possesses highly uniform, ultra-small nanochannels (2–3 nm). This endowed the modified electrode with molecular-level size-exclusion effect, barring large bio-macromolecules (*e.g.* proteins, DNA) from entering the channels and fouling the electrodes. On the other hand, urine samples were diluted by 50-fold before measurement. This dilution effectively minimizes the ionic strength and reduces the concentration of salts. Additionally, commonly salts cannot generate ECL signals under our experimental conditions. Thus, the established method eliminates the need for complex pretreatment procedures, requiring only simple dilution, which greatly simplifies the operational steps.

4. Conclusions

In this work, a highly sensitive ternary ECL sensing system is successfully constructed for the quantitative detection of UA. This platform integrates Uox covalently immobilized on the outer surface of NH_2-VMSF for the specific catalytic generation of H_2O_2 from UA with PtNPs–NGQDs nanocomposites confined within the nanochannels acting as coreaction accelerators. The confined PtNPs–NGQDs exhibit synergistic catalytic capability, achieving a 16.1-fold enhancement of the luminol ECL signal. Benefiting from this signal amplification and the specific recognition of Uox, the proposed sensor achieves highly sensitive UA detection with a low detection limit of 8.1 nM. The facile strategy for sensor fabrication allows for easy change of the immobilized enzyme, showing potential for the development of versatile enzymatic ECL sensing platforms for different metabolites.

Conflicts of interest

There are no conflicts to declare.

Data availability

The authors confirm that the data supporting the findings of this study are available within the article.

Supplementary information (SI) is available. See DOI: https://doi.org/10.1039/d6ra02118b.

Acknowledgements

We acknowledge the financial support from the Zhejiang Provincial Natural Science Foundation of China (LMS25B050001).

References

1 U. A. A. Sharaf El Din, M. M. Salem and D. O. Abdulazim, *J. Adv. Res.*, 2017, **8**, 537–548.
2 M. E. Gherghina, I. Peride, M. Tiglis, T. P. Neagu, A. Niculae and I. A. Checherita, *Int. J. Mol. Sci.*, 2022, **23**, 3188.
3 C. Borghi, E. A. Rosei, T. Bardin, J. Dawson, A. Dominiczak, J. T. Kielstein, A. J. Manolis, F. Perez-Ruiz and G. Mancia, *J. Hypertens.*, 2015, **33**, 1729–1741.
4 F. Pazos Perez, *Contrib. Nephrol.*, 2018, **192**, 116–124.
5 S. Luo, X. Sun, L. Zhang, Y. Miao and G. Yan, *Biosens. Bioelectron.*, 2025, **280**, 117423.
6 J. Wang, S. He, H. Zhang, Z. Yang, Z. Liu, H. Yu and C. Li, *Anal. Chim. Acta*, 2024, **1330**, 343286.
7 K. Ma, L. Yang, J. Liu and J. Liu, *Nanomaterials*, 2022, **12**, 1157.
8 C. Ma, Y. Cao, X. Gou and J. J. Zhu, *Anal. Chem.*, 2020, **92**, 431–454.
9 Z. Shi, T. Zhang, Y. Zhao, Y. Zhou and J. Liu, *Biosens. Bioelectron.*, 2025, **288**, 117828.
10 R. Yu, Y. Zhao and J. Liu, *Nanomaterials*, 2024, **14**, 390.
11 X. Liu, H. Tan, J. Song, L. Tao, X. Wang, C. Zhu and Y. Yu, *Chem. Eng. J.*, 2025, **523**, 168332.
12 X. Luo, T. Zhang, H. Tang and J. Liu, *Front. Nutr.*, 2022, **9**, 962736.
13 J. Li, H. Lin, F. Yan and L. Cui, *Microchim. Acta*, 2026, **193**, 285.
14 M. Liu, Z. Cai and X. Chen, *Chem. Eur J.*, 2025, **31**, e202500007.
15 Z. Tang, K. Wen, Y. Guo, P. Xie, K. Li, Y. Chen, J. L. Liu, R. Yuan and K. Peng, *Anal. Chem.*, 2025, **97**, 10772–10781.
16 C. Zhu, Y. Zhao and J. Liu, *Biosensors*, 2025, **15**, 63.
17 L. Huang, X. Gu and F. Xi, *J. Electroanal. Chem.*, 2026, **1006**, 119896.
18 M. Z. Deng, M. Y. Zhong, M. L. Li, G. Q. Huang, H. He, X. Xiao, R. B. Bai, R. H. Ukwatta, L. Mi, T. T. Zhang, Y. H. Hu, H. C. Shi and Y. Z. Wang, *Anal. Chim. Acta*, 2025, **1361**, 344148.
19 X. Fan, T. Zhang, S. Wang, Y. Jiang, Y. Zhao, F. Yan and F. Xi, *Sens. Actuators, B*, 2025, **439**, 137856.
20 H. Zhang, C. Zhang, H. Qu and F. Xi, *Molecules*, 2023, **28**, 6559.
21 J. Wu, L. Wang, H. Wang, X. Gu, Y. Zhou and F. Xi, *Microchem. J.*, 2025, **209**, 112903.
22 C. Lu, S. Luo, X. Wang, J. Li, Y. Li, Y. Shen and J. Wang, *Coord. Chem. Rev.*, 2024, **501**, 215571.
23 W. Li, R. Yu and F. Xi, *Molecules*, 2024, **29**, 4880.
24 X. Fang, P. Zhang and F. Yan, *J. Electroanal. Chem.*, 2026, **1012**, 120116.
25 X. Zhou, Y. Zou, H. Ru, F. Yan and J. Liu, *Anal. Chem.*, 2024, **96**, 10264–10273.
26 H. Zhang, L. Wu, F. Xi and B. Zhang, *RSC Adv.*, 2025, **15**, 44909–44918.
27 J. Pei, X. Jia, F. Xi and B. Zhang, *Front. Chem.*, 2025, **13**, 1709420.
28 S. Gu, Y. Shao and F. Xi, *ChemistrySelect*, 2026, **11**, e07430.
29 J. Zhao, X. Gu and J. Liu, *Microchem. J.*, 2025, **216**, 114671.
30 Q. Sun, N. Wang, Q. Xu and J. Yu, *Adv. Mater.*, 2020, **32**, e2001818.
31 J. Zhao, S. Yang, F. Xi, X. Yan and J. Wu, *Chem. Eng. J.*, 2025, **508**, 165264.

32 J. Zhao, W. Duan, X. Liu, F. Xi and J. Wu, *Adv. Funct. Mater.*, 2023, **33**, 2308183.
33 J. Gong, H. Tang, M. Wang, X. Lin, K. Wang and J. Liu, *Mater. Des.*, 2022, **215**, 110506.
34 X. Deng, X. Lin, H. Zhou, J. Liu and H. Tang, *Nanomaterials*, 2023, **13**, 239.
35 C. Zhu, H. Wang and J. Liu, *Front. Chem.*, 2025, **13**, 1549927.
36 S. M. Wu, X. Y. Yang and C. Janiak, *Angew. Chem., Int. Ed.*, 2019, **58**, 12340–12354.
37 T. Yan, X. Ma and F. Xi, *RSC Adv.*, 2026, **16**, 23915.
38 C. Lu, X. Fan, F. Xi and Y. Zhou, *Talanta*, 2026, **304**, 129524.
39 X. Fan, L. Wang, H. Wang, L. Huang, J. Lin, X. Gao and F. Xi, *Biosens. Bioelectron.*, 2025, **280**, 117451.
40 W. Zhang, Y. Jiang and F. Xi, *Anal. Chim. Acta*, 2026, **1384**, 344937.
41 X. Fan, J. Wu, T. Zhang and J. Liu, *ChemBioChem*, 2024, **25**, e202400320.
42 L. Wang, S. Gu, F. Yan and C. Shen, *Microchem. J.*, 2026, **220**, 116658.
43 X. Ma, Z. Zhang, Y. Zheng and J. Liu, *Biosensors*, 2024, **14**, 403.
44 J. Huang, T. Zhang, Y. Zheng and J. Liu, *Biosensors*, 2023, **13**, 317.
45 H. Wang, H. Wang and F. Yan, *RSC Adv.*, 2026, **16**, 501.
46 Z. Teng, G. Zheng, Y. Dou, W. Li, C. Y. Mou, X. Zhang, A. M. Asiri and D. Zhao, *Angew. Chem., Int. Ed.*, 2012, **51**, 2173–2177.
47 J. Wu, T. Zhang, X. Jia, J. Li, H. Xie, F. Yan, D. Li and J. Liu, *J. Colloid Interface Sci.*, 2026, **701**, 138721.
48 R. Su, H. Tang and F. Xi, *Front. Chem.*, 2022, **10**, 954748.
49 H. Zhou, Y. Ding, R. Su, D. Lu, H. Tang and F. Xi, *Front. Chem.*, 2022, **9**, 812086.
50 J. Lin, Z. Mao and F. Yan, *Biosensors*, 2026, **16**, 236.
51 A. Walcarius, E. Sibottier, M. Etienne and J. Ghanbaja, *Nat. Mater.*, 2007, **6**, 602–608.
52 D.-H. Lim and J. Wilcox, *J. Phys. Chem. C*, 2012, **116**, 3653–3660.
53 G. He, Y. Song, K. Liu, A. Walter, S. Chen and S. Chen, *ACS Catal.*, 2013, **3**, 831–838.
54 M. G. Trachioti, A. C. Lazanas and M. I. Prodromidis, *Microchim. Acta*, 2023, **190**, 251.
55 Y. Li, X. Gu, J. Zhao and F. Xi, *Molecules*, 2022, **27**, 7379.
56 S. Xu, S. Zhang, Y. Li and J. Liu, *Molecules*, 2023, **28**, 6064.
57 J. Wu, C. Li, J. Zhao and J. Liu, *Microchim. Acta*, 2026, **193**, 134.